Cavitation phenomena in a stagnation point flow

Yuan Lu
Department of Mechanical Engineering,
Johns Hopkins University
Baltimore, MD, USA

Balaji Gopalan
Department of Mechanical Engineering,
Johns Hopkins University
Baltimore, MD, USA

Emine Celik
Department of Mechanical
Engineering, Johns Hopkins
University
Baltimore, MD, USA

Joseph Katz
Department of Mechanical
Engineering, Johns Hopkins
University
Baltimore, MD, USA

David M. Van Wie
Applied Physics Laboratory,
Johns Hopkins University
Baltimore, MD, USA

ABSTRACT

Cavitation phenomena inherently occur in regions with low pressure. Consequently, it seems unlikely that cavitation would develop near the stagnation point of a blunt body flow. However, in recent experiments involving a high-speed bubbly jet impinging on a blunt body, we have observed substantial rapid growth and stretching of bubbles near the stagnation point over a wide range of flow parameters.

Using a high-speed camera we observe that bubbles with initial diameters of tens of microns located very close to the blunt body are being stretched into long "strings" that are generally aligned parallel to the body surface. In-line Digital Holographic Microscopy (DHM) measurements show that the bubble strings are located far from the walls. High resolution 3-D holographic Particle Image Velocimetry (DHM-PIV) is performed to quantify the 3-D flow field near the leading edge of the blunt body. Instantaneous data show vortices being stretched by the local strain field close to the blunt body in an orientation consistent with the appearance of cavitation. These vortices are originated from the turbulent jet upstream. An estimate based on the measured vortex strength and strain field shows that stretching rapidly decreases the pressure in the vortex core below the vapor pressure, explaining the occurrence of cavitation.

INTRODUCTION

The facility in Fig. 1 has been constructed to investigate the application of porous (bubbly) liquid fuels as a means of enhancing fuel reactivity prior to injection into a combustion chamber. The liquid porosity is achieved by mixing it with the gas bubbles that are introduced in the bubble generator. At high void fractions, the sound speed in the bubbly mixture is very low [1]. Thus, as the flow accelerates in the nozzle, the flow may become supersonic, and susceptible to occurrence of shock waves in the test section, which may also compress the bubbles. Consequently, we have inserted a blunt body in the test section to generate an adverse pressure gradient that would facilitate shock formation immediately downstream of the jet [2]. As it has turned out, the flow has been dominated by cavitation, including an unusual phenomenon of cavitation near the stagnation point of the blunt body. This cavitation involves rapid growth and stretching of bubbles as the high-speed turbulent bubbly jet impinges on the blunt surface. This paper describes our effort to understand these observations.
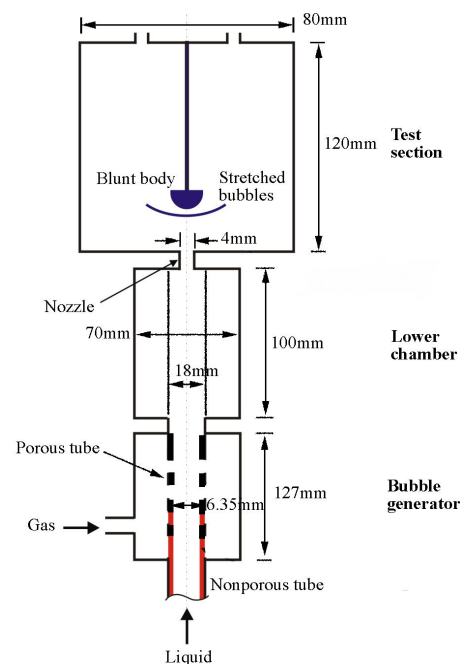

Figure 1: Sketch of the high-speed bubbly jet facility.

Cavitation commonly occurs when the local pressure in a liquid falls below the vapor pressure, either due to a high speed flow or in an acoustic field [1,3]. However, since a steady flow towards the stagnation point of a solid body decelerates, the mean pressure increases there [4]. Hence, the vicinity of a stagnation point is the last place where one expects to see violent cavitation. Inherently, the prerequisite of low pressure as a condition for cavitation inception must be satisfied. Thus, the pressure at the locations of rapidly growing stretched bubbles must be low. Vortices have low pressure in their cores and they are dominant contributors to cavitation inception in many processes [5]. Cavitating vortical structures vary from the relatively stable tip vortices on propellers and hydrofoils [3,6,7], to randomly distributed eddies in turbulent shear flows [8-10], jets [5,11] and boundary layers [12,13].

In the current experiments cavitation develops as turbulent eddies generated by a jet are stretched by a strain field associated with a blunt body located downstream of this jet. Extension of these vortices intensifies the vorticity in the vortex core [4], reducing the pressure there. Previous studies of turbulence near the leading edge of blunt bodies [14,15] have shown that straining preferentially aligns eddies parallel to the blunt body's surface and enhances heat transfer. In the present study we observe cavitating vortices generally aligned parallel to the surface. High-speed imaging is first used to examine the process of bubble stretching. Then, we use DHM-PIV measurements to quantify the 3-D flow field near the stagnation point of the blunt body, and examine whether the local strain field can indeed stretch the vortices to a level that would cause cavitation inception.

EXPERIMENTAL SET UP

The bubbly jet facility is illustrated in Fig. 1. The bubbles are introduced upstream of the jet by forcing gas through a porous tube in the bubble generator. The volume fraction of the gas can be controlled in a range of 0-50%. The size of the bubbles is varied in the range of several microns to 2 mm by premixing the water with a surfactant (3-pentanol), and by varying the flow velocity in the bubble generator. The lower chamber is transparent so that the bubble size and distribution can be observed and measured. The bubbly flows accelerate through a rectangular nozzle with depth of D=2 mm. The nozzle widths and shape can be readily varied to suit different experiments. Currently, a 4 mm wide nozzle is used. The depth of the transparent test section is also 2 mm, i.e. equal to that of the nozzle. A semi-circular blunt body with diameter of 6 mm is located at 8.5 mm away from the nozzle exit, and extends over the entire 2 mm depth. The region covering the nozzle and the test section is transparent, enabling observations at any point on the flow within the nozzle and in the test section.

During experiments, a high-speed water jet with or without bubbles is injected through the nozzle and impinges on the blunt body. The flow velocity in the nozzle (V) varies from 7.7 m/s to 35 m/s. The corresponding Reynolds number based on V and D ($Re=VD/\nu$, ν is the kinematic viscosity) varies from 15400 to 70000. The pressure in the test section can be varied from nearly vacuum to about 20 atm.

Using a high speed digital camera with (maximum) resolution of 1k×1k pixels, and incandescent light forward illumination (500 W), we record snapshots of the bubbles at full resolution (1 μm/pixel) to visualize the stretched bubbles, and record high speed movies at 50000 f/s at a resolution of 64×256 pixels (20 μm/pixel) to examine the time evolution of the bubble growth.

In-line DHM is capable of obtaining the locations of bubbles not only in the lateral but also in the depth dimension [16,17]. To determine the depth location with respect to the walls and shape of the stretched bubbles, we record pairs of digital in-line holograms using a 2k×2k pixels CCD camera, which focuses on the region located near the stagnation point. The optical setup is illustrated in Fig. 2. Several magnifications with pixel resolution in a range of 0.54-1.1 μm/pixel are used. The focal plane of the objective is located just outside the sample volume, denoted in Fig. 2 with a red dash-line. The time interval between exposures is 1 μs. The holograms are reconstructed numerically in several planes along the optical axis using the Fresnel approximation [17,18].
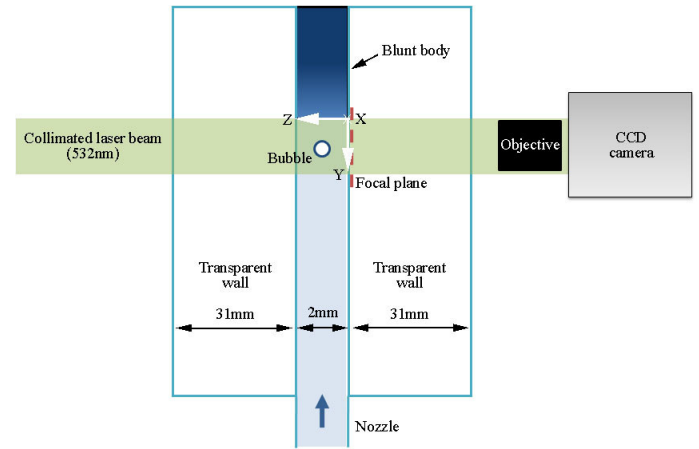

Figure 2: Optical setup of digital in-line holography (lateral view).

DHM-PIV is a volumetric technique that can measure the 3-D instantaneous velocity fields at a resolution of ~20 – 40 μm [19]. We perform DHM-PIV measurements near the leading edge of the blunt body surface at V=7.7 m/s, using the same optical setup as described before, but without bubbles. Instead, the water is seeded homogeneously with 2-5 μm polyamide particles. The in-pair time interval is 3 μs, and the pixel resolution is 0.75 μm/pixel. Data analyses focus on a 1k×1k window with its upper left corner coinciding with the stagnation point, and left edge coinciding with the center-plane of the blunt body (Fig. 3). The dimension of the sample volume is 0.768 mm × 0.768 mm × 2 mm, the latter being the depth. After reconstruction, a 3-D segmentation procedure is applied to determine the 3-D coordinates of each particle [17,19]. Particle tracking is then used to measure the velocity of each particle from its displacement in successive frames. The algorithms for particle tracking are described in detail in ref. [19]. The number of vectors in individual realizations varies from 1000 to 2000. The unstructured vectors are then interpolated into a regular grid based on a first order Taylor expansion [19], rendering 32×32×83 structured vectors, with vector spacing of 24 μm. The velocity gradients are directly

2

obtained from the interpolation procedure. During experiments, over 200 pairs of holograms have been recorded, but only 12 3-D velocity distributions have been processed and analyzed. Data analysis is still in progress.
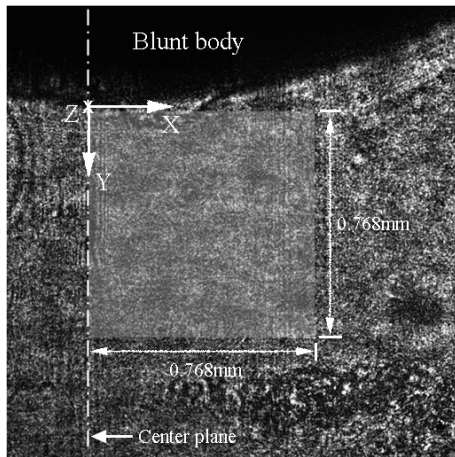

Figure 3: A sample microscopic hologram and the region analyzed to obtain 3-D velocity distributions. The stagnation point is located at the origin of the coordinate system.

RESULTS

The snapshots in Fig. 4 shows sample stretched bubbles in different flow velocities with heavy seeding of bubbles. In all cases, the string-like bubbles aligned parallel to the blunt body surface are clearly visible. The diameters of the bubble strings decrease with increasing velocity. Note that the space between the strings and the blunt body surface contains a few bubbles due to pressure-induced "rejection" or screening [20].
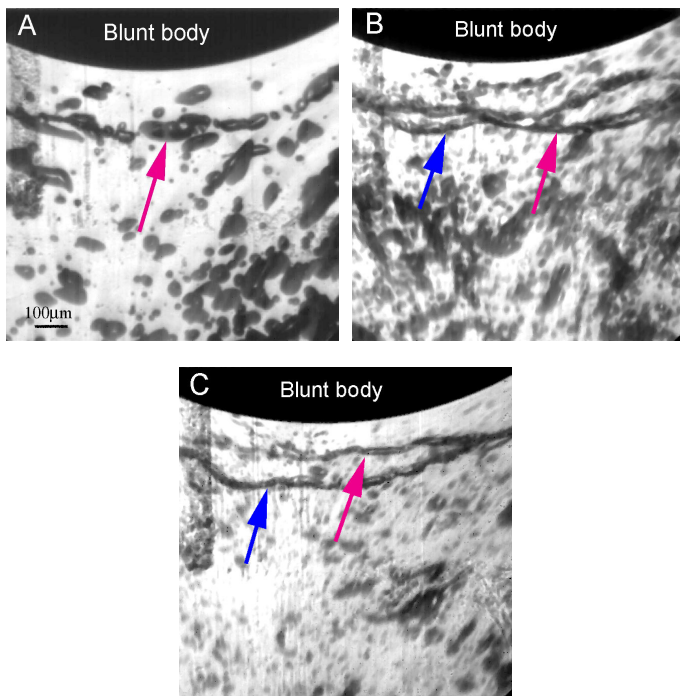

Figure 4: Bubble strings (indicated by the arrows) near the stagnation point at (A) $V=10$ m/s, (B) $V=25$ m/s, (C) $V=35$ m/s.

To visualize the process of the bubble stretching, we have reduced the concentration of bubbles in the facility and recorded images at 50000 f/s. Fig. 5 shows five successive sample images of a bubble (indicated by the arrow) with initial diameter of about 80 μm being stretched into long a "string" aligned parallel to the body surface. After 80 μs, the cross-section diameter of this string remains nearly unchanged, while its length is about seven times the initial diameter. Thus, the axial growth rate of this bubble is about 6m/s, which is comparable to the jet velocity. The high-speed movies also show that the bubble is spinning while growing, clearly suggesting that it is located in a core of a vortex. It should be noted that rapid bubble growth and stretching occur near the leading edge of the blunt body regardless of whether there is cavitation in the nozzle upstream.
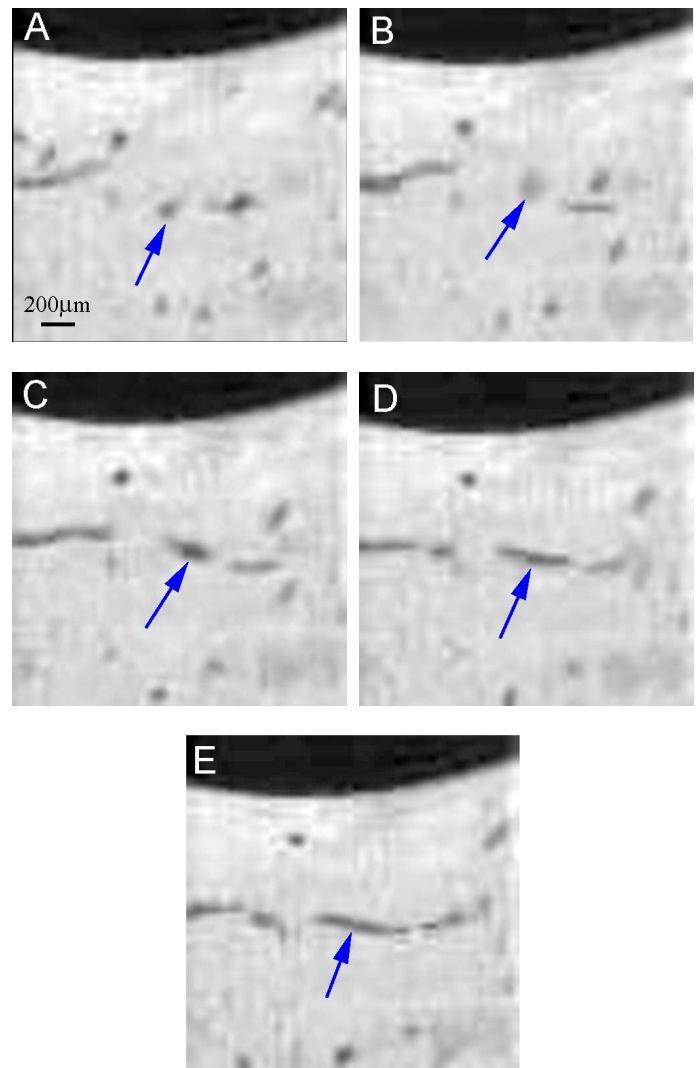

Figure 5: A sequence of high-speed movie images showing the growth and stretching of a microbubble with initial diameter of 80μm located close to the stagnation point. The time interval between successive frames is 20 μs. $V=7.7$ m/s.

To determine the depth locations of these stretched bubbles, we perform in-line DHM measurements. Here again, a

very small number of bubbles is introduced to obtain clear holograms. Fig. 5 shows a representative reconstructed image of an in-focus elongated bubble, which is recorded at a pixel resolution of 0.54 μm/pixel. The diameter of this bubble is 38 μm, while its length is 754 μm, rendering an aspect ratio (length/diameter) of almost 20. All parts of the bubble string are in focus, indicating that it is aligned perpendicular to the optical axis, i.e. parallel to the walls. This in-focus image is obtained by reconstructing the hologram at Y=1.3 mm, indicating that the cavitating process occurs far from the walls. The location of bubble growth away from the side-windows has been repeatedly confirmed by reconstructing numerous other holograms, indicating that the underlying flow phenomenon is not related to these surfaces.

The pair of exposures also enables us to better visualize the bubble growth. Fig. 7 shows a pair of in-focus images of an expanding bubble at a pixel resolution=1.1 μm/pixel. The initial diameter of this bubble is about 9 μm (Fig. 7A). In 1 μs, this bubble expands to an ellipsoid with a major axis length of 33 μm (Fig. 7B), i.e. the axial growth rate is about 24 m/s, which is still comparable to the jet velocity. Fig. 7 contains also a couple of other elongated bubbles.
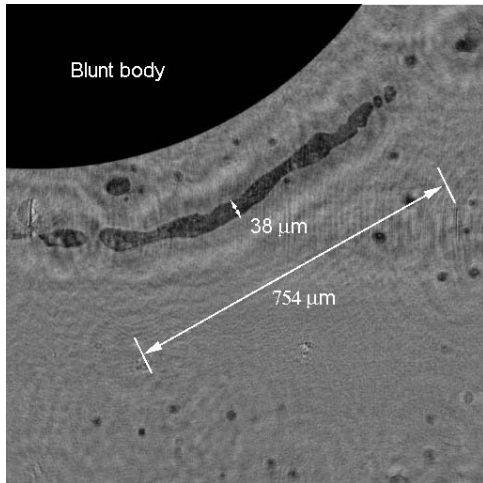

Figure 6: A reconstructed holographic image at Y=1.3 mm shows an in-focus elongated bubble. V=7.7 m/s.
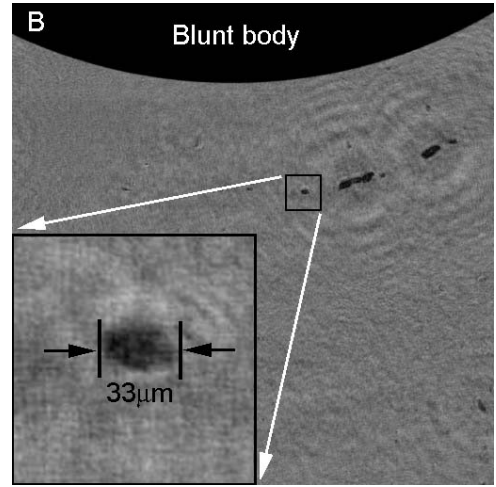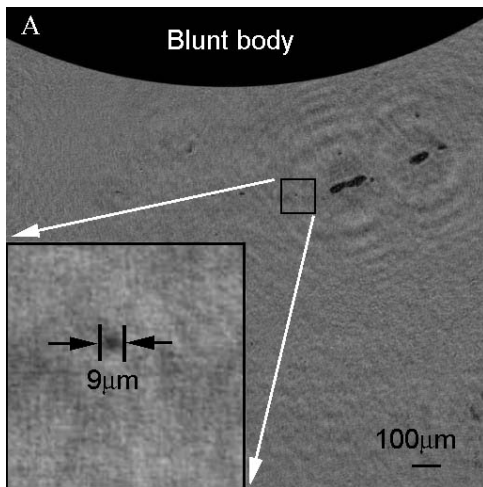

Figure 7: An in-focus reconstructed image pair showing the rapid growth of a microbubble. Inset at the lower left corner of each image shows the close-up of the section enclosed by the small box. The time interval between the exposures is 1 μs; V=30 m/s.

As described before, DHM-PIV measurements provide the instantaneous 3-D velocity fields, as sample of which is shown in Fig. 8. Recall that the blunt body is located above the sample volume, with its stagnation point located at X=0, Y=0. We use the 3-D data to determine whether strong vortical structures exist near the stagnation point, and whether the strain field can stretch them to a level that would cause cavitation. First, we use the 3-D data to identify the vortical structures. For the data cube shown in Fig. 8, Fig. 9A shows the (total) vorticity magnitude (normalized by V/D) in two Y-Z planes as well as the sample vortex lines passing through the high vorticity region at about Z=1.1 mm. Fig. 9B shows the velocity and vorticity distribution (colour contours) in an X-Y plane at Z=1.1 mm. An elongated vortical structure aligned (almost) along the X direction, as indicated by the vortex lines, can be clearly identified.

To reveal the effect of the local strain field on the vortex, we calculate $|\cos(\theta_1)|$, where θ_1 is the angle between the vorticity vector $\boldsymbol{\omega}$ and the most extensive eigenvector, $\mathbf{e}_1$, of the strain rate tensor $\mathbf{S}$ [21,22]. Fig. 10 shows the vorticity vectors, the vorticity magnitude and the distribution of $|\cos(\theta_1)|$ at the same depth location as in Fig. 9B. In the region of peak vorticity, which is denoted by an white arrow in Fig. 10, the vorticity peak overlaps with the high $|\cos(\theta_1)|$ region. Consequently, this part of the vortex forms a 37° angle with the most extensive eigenvector, whose characteristic magnitude is 50000 1/s. The vorticity component aligned with $\mathbf{e}_1$ is being stretched by it. The intermediate strain rate also contributes to vortex stretching, but due to its relatively small magnitude, roughly an order of magnitude smaller than the most extensive strain rate, its effect is weak. Of the 12 data sets that we have analyzed to date, only one more realization captures a powerful vortex closely aligned with $\mathbf{e}_1$. The other distributions contain relatively weaker vortices without such an alignment. As this vortex is stretched along its axis, the vorticity in its core intensifies, resulting in a lower core pressure. In the next

section, we use the current data to estimate whether vortex stretching by the measured strain may cause cavitation.
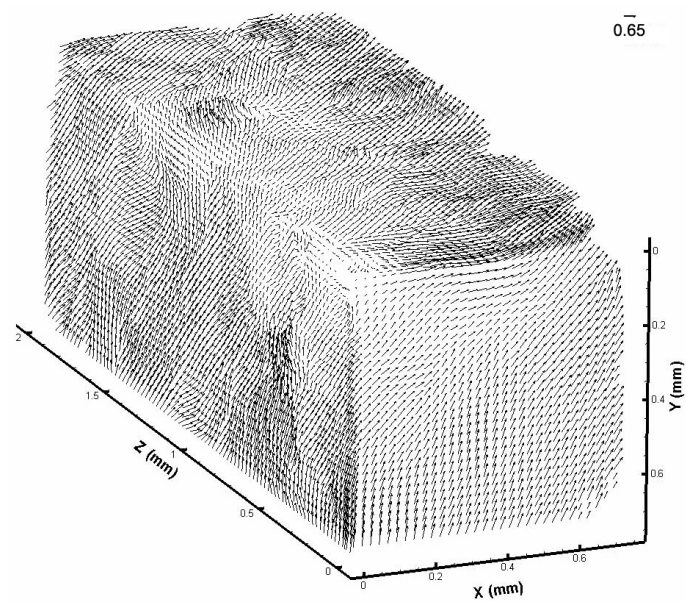

Figure 8: A sample instantaneous 3-D structured velocity field of the flow near the stagnation point containing 32×32×83 vectors. A reference vector normalized by V (7.7 m/s) is shown at the upper right corner.

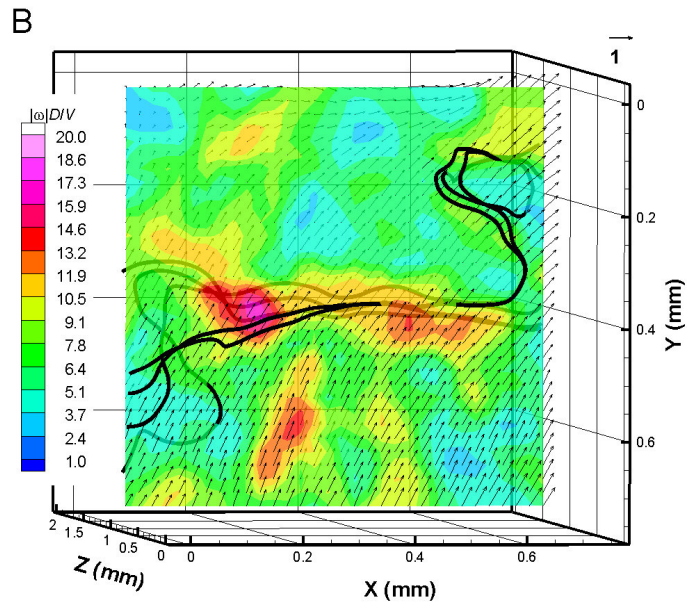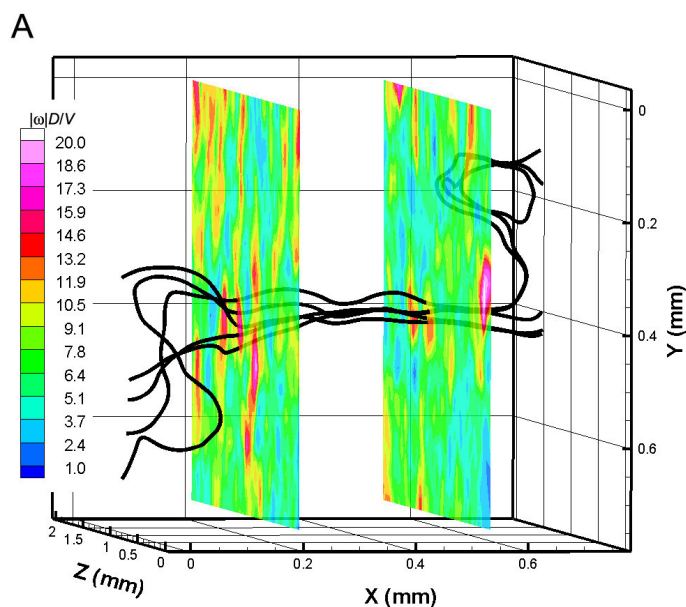**Figure 9:** An instantaneous vortical structure at Y≈0.4 mm, Z=1.1 mm. (A) Normalized vorticity magnitude (color contours) in two Y-Z planes and sample vortex lines passing through the high vorticity region. (B) Velocity and normalized vorticity distribution (colour contours) in an X-Y plane located at Z=1.1 mm. Vectors show the 3-D velocity with grey arrows pointing into the page (positive w), and a reference normalized by V shown at the upper right corner.

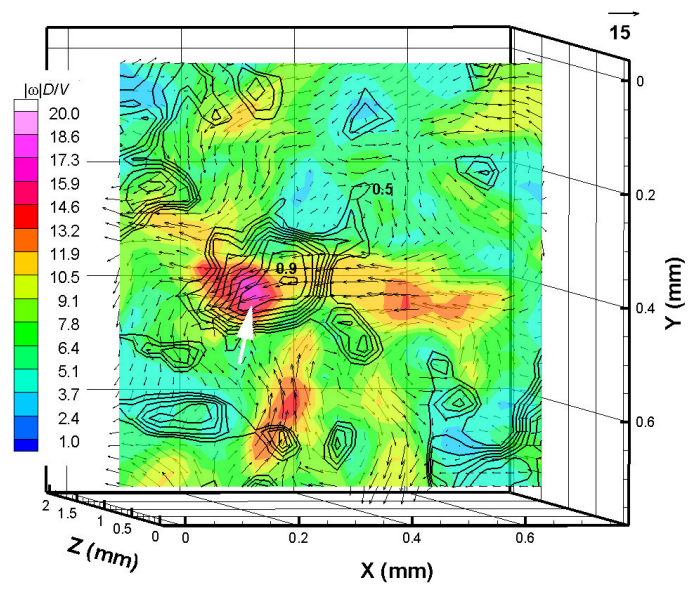**Figure 10:** Vorticity vectors, normalized vorticity magnitude (colour contours) and $|\cos(\theta_1)|$ (black line contours). The value of $|\cos(\theta_1)|$ at the outermost contour is 0.5, and the incremental increase between lines is 0.05. The white arrow denotes the peak vorticity region, corresponding to the data presented in Fig. 9. A normalized reference vorticity vector is shown at the upper right corner.

5

DISCUSSION

Based on the 3-D data obtained from the DHM-PIV measurements, we roughly estimate the effect of vortex stretching on the local pressure drop, assuming an inviscid stretching, relying on the high Reynolds number and short time involved. Based on pressure measurements upstream of the nozzle, and the measured jet velocity, and neglecting losses, the absolute pressure in the nozzle is 2.1 atm, and the stagnation pressure near the leading edge of the blunt body, p_s, is about 2.4 atm. This is a conservative estimate due to losses especially at the exit from the nozzle. In the region of 3-D velocity measurements, the characteristic velocity is ~5 m/s, i.e. the static pressure is 2.3×10^5 Pa. However, for this velocity, the difference between stagnation and static pressure is small, so we will continue using p_s. To achieve vapor pressure in the vortex core (2330 Pa at 20ºC), the pressure drop due to vortex stretching should be nearly equal to p_s.

Assume an axisymmetric flow near the vortex center, the pressure gradient can be approximated as

$$\frac{\partial p}{\partial r} = \frac{\rho V_\theta^2(r)}{r}, \tag{1}$$

where $V_\theta(r)$ is the circumferential velocity component at a distance r from the vortex center. Assuming a Rankine vortex, the velocity at the edge of a vortex core with radius a can be approximated as:

$$V_\theta(a) = \frac{\Gamma}{2\pi a}, \tag{2}$$

where Γ is the circulation. Since $\Gamma = \int_A \boldsymbol{\omega} \cdot \mathbf{n} dA = \varpi(\pi a^2)$, where ϖ is the mean vorticity magnitude over a cross section area of the vortex tube A, we obtain

$$p_s - p(a) \approx \frac{\rho}{8}(\varpi a)^2. \tag{3}$$

The inviscid vorticity transport equation in the eigenframe can be expressed as

$$\frac{d\omega_k}{dt} = s_k \omega_k \quad (k = 1, 2, 3) \tag{4}$$

where s_k is the eigenvalue of $\mathbf{S}$, with $s_1 \geq s_2 \geq s_3$ and $s_1+s_2+s_3=0$ for an incompressible flow. Neglecting the time variations in s_k for a brief period, the solution of eq. (4) is

$$\omega_k(t + \Delta t) = \omega_k(t) \exp(s_k \Delta t). \tag{5}$$

In homogenous isotropic turbulence the vorticity is preferentially aligned with the intermediate strain eigenvector [22,23]. However, in our case, the turbulence fed by the jet is not isotropic, and in fact, the core of the vortex in the sample shown (as well as in another case out of 12 with a strong vortex) seems to be aligned close to $\mathbf{e}_1$. Accounting for $\theta_1(t)$, at an given instant, the averaged $\omega_1(t)$ over A is approximately $\varpi(t)|\cos[\theta_1(t)]|$, giving,

$$\varpi(t + \Delta t) \approx \frac{|\cos[\theta_1(t)]|}{|\cos[\theta_1(t + \Delta t)]|} \varpi(t) \exp(s_1 \Delta t). \tag{6}$$

Combining Eq. (3) and (6),

$$p_s - p(a, t + \Delta t) \approx \frac{|\cos[\theta_1(t)]|}{|\cos[\theta_1(t + \Delta t)]|}[p_s - p(a, t)] \exp(s_1 \Delta t), \tag{7}$$

implying that the pressure drop in the vortex core increases exponentially with vortex stretching. Accordingly, the time required for the pressure in the vortex core to drop to the vapor pressure [$p(a, t+\Delta t) = p_v$] is:

$$\Delta t = \frac{1}{s_1} \ln\left[\frac{|\cos[\theta_1(t + \Delta t)]|}{|\cos[\theta_1(t)]|} \frac{p_s - p_v}{p_s - p(a, t)}\right]. \tag{8}$$

Setting (somewhat arbitrarily) a threshold of 70% of the peak vorticity, i.e. a threshold of $|\boldsymbol{\omega}| \approx 50000$ 1/s, the boundary of this vortex can be defined, and the values of ϖ, a and s_1 can be calculated. We obtain $\varpi(t) \approx 6.3 \times 10^4$ 1/s, $a(t) \approx 100$ μm, $|\cos[\theta_1(t)]| \approx 0.8$, and $s_1 \approx 5 \times 10^4$ 1/s. Using eq. (3), $p_s - p(a,t) \approx 4960$ Pa, i.e. a very small difference; therefore, the vortex, at its current state, is far from a cavitation condition.

Neglecting the changes of the other vorticity components, since they are not stretched to the same extent (ω_2 changes very little, and ω_3 decreases due to compression), after stretching, $\cos[\theta_1(t+\Delta t)]| \approx 1$. According to eq. (8), the time that it would take for the core pressure to drop below vapor pressure is 81 μs. Since the magnitude of the velocity is about 5 m/s at the vortex location, it would be convected only by about 405 μm (286 μm vertically and by the same amount horizontally) during this period, very little compared to the flow length scales, ~3 mm (the radius of the blunt body). However, its mean vorticity would increase to 2.9×10^6 1/s, and its core radius will decrease to 15 μm. With the resulting low pressure, entrained microbubble would cavitate. Clearly, the present simplified analysis involving measured vortex strength and the strain field to which it is exposed suggests that vortex stretching can readily decrease the vortex core pressure below the vapor pressure.

CONCLUSION

This paper demonstrates that as a turbulent flow impinges on the surface of a blunt body, cavitation may occur near the leading edge, in spite of the high mean pressure there. The cavitation appears as series of elongated vortices with vaporous cores that are generally aligned parallel to the surface. Vortices that are an inherent part of the turbulent flow may have different orientations. However, the strain field in the vicinity of the stagnation point stretches these vortices and preferentially aligns them in a direction parallel to the surface. Extension of these vortices intensifies the vorticity and reduces the pressure in their cores. If the vortex and strain rate are sufficiently powerful, the pressure in its core may decrease below the vapor pressure, creating conditions prone to cavitation inception. In the present example, the turbulence is generated by a jet located upstream of the stagnation point. We use high resolution, three dimensional velocity distributions,

obtained using DHM-PIV, to demonstrate that turbulent vortices aligned parallel to the surface indeed exist, and that the strain field is adequately powerful to stretch them axially to a cavitation condition in less than 0.1 ms.

Of course, for cavitation to occur near a stagnation point, the flow must contain sufficiently powerful turbulent eddies. One can envision other scenarios, with, e.g., coherent turbulent vortices generated by a rudder or ship hull being stretched by the stain field at the leading edge of a propeller blade. Recall that numerical simulations [14,15,24] have shown that as a turbulent flow impinges on a solid boundary in a stagnation point flow or on the leading edge of a turbine blade, the eddies become elongated and aligned parallel to the surface as they are being stretched. Thus, the presently observed phenomenon is not uncommon.

ACKNOWLEDGMENTS

NOMENCLATURE

$\mathbf{e}_k$ — eigenvector of $\mathbf{S}$, k = 1,2,3
P — pressure
p_s — stagnation pressure
p_v — vapor pressure
s_k — eigenvalue of $\mathbf{S}$
t — time
u, v, w — velocity components in X, Y, Z directions
D — nozzle depth
Re — Reynolds number
$\mathbf{S}$ — strain rate tensor
V — jet velocity
Γ — circulation
$\boldsymbol{\omega}$ — vorticity vector
ϖ — mean vorticity magnitude
ω_k — component of $\boldsymbol{\omega}$ in the eigenframe
θ_k — angle between $\boldsymbol{\omega}$ and $\mathbf{e}_k$
ν — kinematic viscosity

REFERENCES

[1] Brennen, C. E. 2005, *Fundamentals of Multiphase Flow*. Cambridge University Press.

[2] Celik, E., Katz, J. 2009, "Investigation of the formation of microbubbly liquid fuel," *11th International Symposium on Gas-Liquid Two-Phase Flows*, ASME: Colorado, USA, FEDSM2009-78546.

[3] Arndt, R. E. A. 1981, "Cavitation in fluid machinery and hydraulic structures". *Annual review of fluid mechanics*,13, 273-328.

[4] Batchelor, G. K. 1967, *An introduction to fluid dynamics*. Cambridge University Press, New York.

[5] Arndt, R. E. A. 2002, "Cavitation in vortical flows," *Annual review of fluid mechanics*, 34, 143-175.

[6] Arndt, R. E. A., Arakeri, V. H., Higuchi, H. 1991, "Some observations of tip-vortex cavitation," *Journal of fluid mechanics*, 229, 269-289.

[7] Choi, J., Ceccio, S. L. 2007, "Dynamics and noise emission of vortex cavitation bubbles," *Journal of fluid mechanics*, 575, 1-26.

[8] O'Hern, T. J. 1991, "An experimental investigation of turbulent shear flow cavitation," *Journal of fluid mechanics*, 1990, 365-391.

[9] Liu, X., Katz, J. 2008, "Cavitation phenomena occurring due to interaction of shear layer vortices with the trailing corner of a 2D open cavity," *Physics of fluids*, 20, 041702.

[10] Katz, J., O'Hern, T. J. 1986, "Cavitation in the shear layer behind a two dimensional sharp-edge plate," *J Fluids Eng*, 108, 373-376.

[11] Gopalan, S., Katz, J., Knio, O. 1999, "The flow structure in the near field of jets and its effect on cavitation inception," *Journal of fluid mechanics*, 398, 1-43.

[12] Gopalan, S., Katz, J. 2000, "Flow structure and modeling issues in the closure region of attached cavitation," *Physics of fluids*, 12, 895-911.

[13] Franc, J. P., Michel, J. M. 1985, "Attached cavitation and the boundary layer: experimental investigation and numerical treatment," *Journal of fluid mechanics*, 154, 63-90.

[14] Bae, S., Lele, S. K., Sung, H. J. 2003, "Direct numerical simulation of stagnation region flow and heat transfer with free-stream turbulence," *Physics of fluids*, 15, 1462-1484

[15] Xiong, Z., Lele, S. K. 2007, "Stagnation-point flow under free-stream turbulence," *Journal of fluid mechanics*, 590, 1-33.

[16] Vikram, C. S. 1992, *Particle field holography*. Cambridge University Press.

[17] Sheng, J., Malkiel, E., Katz, J. 2006, "Digital holographic microscope for measuring three-dimensional particle distributions and motions," *Applied Optics*, 45, 3893-3901.

[18] Milgram, J., H., Li, W. 2002, "Computational Reconstruction of Images from Holograms," *Applied Optics*, 41, 853-864.

[19] Sheng, J., Malkiel, E., Katz, J.. 2008, "Using digital holographic microscopy for simultaneous measurements of 3D near wall velocity and wall shear stress in a turbulent boundary layer," *Experiments in fluids*;, 45, 1023-1035.

[20] Johnson, V. E. J., Hsieh, T. 1966, "The influence of the trajectories of gas nuclei on cavitation inception," *Proc 6th ONR Symp On Naval Hydrodynamics*, 163-182.

[21] Hamlington, P. E., Schumacher, J., Dahm, W. J. A. 2008, "Local and nonlocal strain rate fields and vorticity alignment in turbulent flows," *Physical Review E*, 77, 026303.

[22] Tao, B., Katz, J., Meneveau, C. 2002, "Statistical geometry of subgrid-scale stresses determined from holographic particle image velocimetry measurements, *Journal of fluid mechanics*, 457, 35-78.

[23] Jimenez, J. 1992, "Kinematic alignment effects in turbulent flows," *Physics of fluids A*, 4, 652-654.

[24] Van Fossen, G. J., Simoneau, R. J. 1987, "A study of the relationship between free-stream turbulence and stagnation region heat transfer," *J. Heat Transfer*, 109, 10-15.